Chapter

Oxygen Vacancies in Spinels

Jiacheng Li

Abstract

Spinel oxides, with the general formula AB_2O_4, are a class of ternary transition metal compounds renowned for their diverse elemental composition and tunable electronic properties. Their cubic crystal structure, belonging to the Fd-3 m space group, features metal ions in both tetrahedral and octahedral coordination centers, which can be manipulated to achieve different catalytic functionalities. This review focuses on the impact of oxygen vacancies on the structural and catalytic properties of spinel oxides and the various strategies to introduce these vacancies. The formation of oxygen vacancies, facilitated through heat treatment, chemical reduction, etching, doping, and composite formation, has been shown to significantly enhance the conductivity, redox potential, and catalytic activity of spinel oxides. These vacancies act as active sites, promote electron/ion transfer, and lower activation energies for various catalytic reactions. Characterization techniques such as X-ray photoelectron spectroscopy (XPS), electron paramagnetic resonance (EPR), and density functional theory (DFT) calculations provide comprehensive insights into the distribution, concentration, and electronic structure modifications due to oxygen vacancies. Theoretical calculations, in particular, underscore the pivotal role of vacancies in stabilizing reaction intermediates and reducing energy barriers. This review synthesizes the current understanding of oxygen vacancies in spinel oxides and highlights the potential for defect engineering as a strategy to optimize catalysts for applications in energy storage, environmental catalysis, and electrochemical reactions.

Keywords: spinels, vacancies, catalysis, copper, spectroscopy

1. Introduction

Spinel, a ternary transition metal ion compound, boasts a rich elemental composition and a unique electronic structure, with a structure that is both variable and adjustable. It is represented by the chemical formula AB_2O_4, where A and B sites are occupied by transition metal elements, and it belongs to the Fd-3 m space group of the cubic crystal system [1]. Research on spinel transition metal oxides is extensive, focusing on the distribution of metal ions within the crystal structure, which are found in tetrahedral and octahedral coordination centers. The valence states of cations differ in these environments, while anions are situated at the vertices of the polyhedron. In the spinel geometry, only half of the octahedral sites and one-eighth of the tetrahedral sites are filled with metal cations, leaving ample space for the accommodation of external metal cations.

Spinel can exhibit three distinct crystal structures based on the coordination environments of A and B cations. A normal spinel structure occurs when all divalent

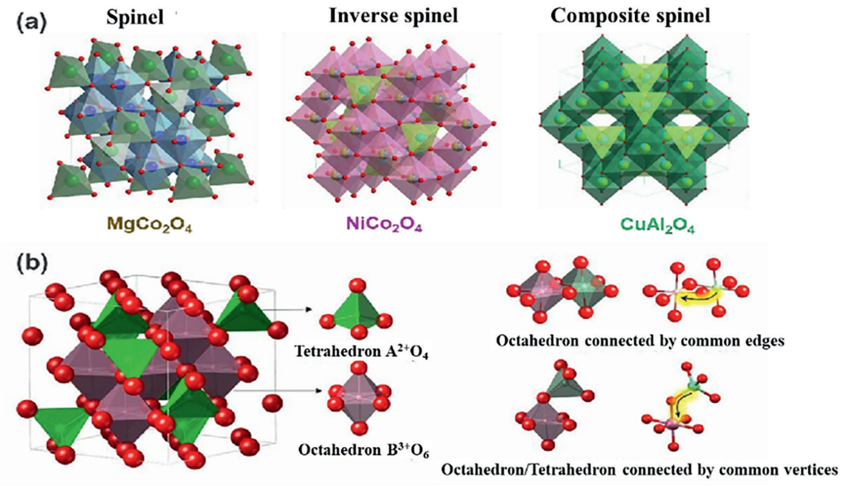

Figure 1.
Structural characteristics of spinel oxide. (a) Explain the categories of spinel oxides using several typical spinel oxides as representatives. Among them, $MgCo_2O_4$ *is spinel, with* Mg^{2+} *and* Co^{3+} *occupying tetrahedral and octahedral centers, respectively;* $NiCo_2O_4$ *is an inverse spinel, with half of* Co^{3+} *occupying tetrahedral centers and the other half of* Co^{3+} *and all* Ni^{2+} *occupying octahedral centers;* $CuAl_2O_4$ *is a composite spinel, with* Cu^{2+} *and* Al^{3+} *mixed to occupy tetrahedral and octahedral sites. (b) Coordination structure in spinel. Among them, octahedra are connected to each other through a common edge method, and octahedra and tetrahedral positions are connected to each other through a common vertex method.*

metal cations occupy the tetrahedral sites (A site) and all trivalent metal cations occupy the octahedral sites (B site). An inverse spinel structure is identified when half of the trivalent metal cations occupy the tetrahedral sites (A site), while the other half, along with divalent metal cations, occupy the octahedral sites (B site). A mixed spinel structure arises when both tetrahedral and octahedral sites are occupied by a mixture of divalent and trivalent metal cations. The connectivity of the Oh sites by common edges and the connection of Td and Oh sites by common vertices provide a theoretical foundation for modulating the electronic structure and catalytic performance of catalysts through the rational design of spinel oxide structures [2].

Typically, site A can be occupied by divalent cations such as Fe^{2+}, Mn^{2+}, Zn^{2+}, and Co^{2+}, while site B can be occupied by trivalent metal ions like Fe^{3+}, Al^{3+}, Cr^{3+}, Cu^{3+}, Ni^{3+}, etc. The unit cell, as depicted in **Figure 1(a)**, contains 24 metal ions (8 A^{2+} and 16 B^{3+}) and 32 O^{2-}. The O^{2-} ions are densely packed in a cubic form, creating a multitude of polyhedral gaps. With six oxygen ions forming octahedral gaps and four forming tetrahedral gaps, cations are positioned within these gaps in the crystal structure. However, the lattice contains as many as 96 gaps, which is significantly more than the number of cations. Consequently, not all gaps can be filled by cations, resulting in a multitude of vacant gaps. These excess gaps facilitate the regulation of metal ion diffusion and the formation of vacancies.

2. Definition and effects of oxygen vacancies on spinel

Perfect spinel crystals with stoichiometric ratios often display significant isotropic physical and chemical properties. The introduction of trace defects, such as oxygen vacancies, can profoundly alter these properties, including conductivity, band structure, adsorption/desorption, and thermodynamics. These defects can regulate the electronic density of states and surface properties of nanomaterials, which is particularly crucial for catalytic applications. Defect engineering creates unsaturated active sites for molecular adsorption by introducing oxygen vacancies, effectively enhancing reaction activity as demonstrated in various studies [3].

Oxygen vacancies in spinel oxides are formed by the absence of lattice oxygen on the surface of metal oxides. These vacancies possess abundant localized electrons that can influence the physical and chemical properties of the metal oxide, including redox capability, resistive switching, and magnetism. They can provide a large number of dangling bonds for intermediates in electrocatalytic reactions, thereby improving electrocatalytic performance through various mechanisms, such as influencing the evolution of active sites, altering metal valence states, regulating electronic structures, changing metal-oxygen bond lengths, and reducing reaction activation energies [4–6]. The presence of oxygen vacancies in spinel significantly enhances the catalyst's ability to adsorb and activate reactive species, accelerating the production of target products and thereby increasing the activity and selectivity of catalytic reactions. Moreover, oxygen vacancies can optimize the pore structure of the spinel, facilitating the in-situ formation of highly active sites on the catalyst surface.

In general, the introduction of oxygen vacancies in spinel materials can influence catalytic performance through various mechanisms, such as activating reactant molecules, enhancing active sites, improving electronic structure, and increasing catalytic selectivity. Therefore, designing and thoroughly analyzing the oxygen vacancy structure in spinel catalysts is crucial for optimizing catalytic efficiency.

3. Preparation methods and catalytic performance of oxygen vacancies

3.1 Heat treatment method

Heat treatment is a straightforward and common method for regulating oxygen vacancies. Xie et al. prepared ultra-thin nanosheet structured $NiCo_2O_4$ samples and obtained two types of nanosheets: one rich in oxygen vacancies (NiCo-r) and the other with few oxygen vacancies (NiCo-p) through calcination in air and oxygen atmospheres [7]. Electrochemical OER tests conducted in a 1 M KOH solution revealed that the NiCo-r sample had the lowest overpotential of 0.32 V and an exceptionally high current density of 285 $mA \cdot cm^{-2}$ at a potential of 0.8 V. In ultra-thin nanosheets, oxygen vacancies are structurally confined, which enhances the reactivity of active sites and effectively reduces the adsorption energy of water, promoting surface reactions and significantly improving OER activity.

Xu et al. controlled the synthesis temperature of spinel $MnCo_2O_4$ to obtain a series of samples with different Mn valence states [8]. The overpotential exhibited a volcanic trend with the valence state of the element, with the cation valence state in octahedral coordination playing a dominant role in catalytic activity. This was related to the electron filling of the oxide's e_g orbital. Research on the electron occupancy rate of e_g orbitals in spinel oxides indicates that the electron occupancy rate is a crucial indicator for catalyst selection and can effectively regulate the valence state of metal atoms by altering oxygen vacancies. Chen et al. successfully synthesized hollow $NiCo_2O_4$ nanoparticles with abundant oxygen vacancies and a porous structure by combining solvent heat and annealing [9]. The $NiCo_2O_4$-450-V_o, with its hollow porous structure, demonstrated dual functional electrocatalytic performance for

MOR and ORR under alkaline conditions. The enhancement in the performance of $NiCo_2O_4$-450-V_o is attributed to its morphological structure and active sites. Oxygen defect engineering can effectively modulate the electronic structure of the $NiCo_2O_4$ material, improving its intrinsic activity, while the hollow and layered porous structure can facilitate reaction kinetics.

3.2 Reduction method

Spinel samples rich in oxygen vacancies can be prepared using chemical reducing agents. Lu et al. reduced $CoFe_2O_4$ on carbon nanotubes with $NaBH_4$ and observed a significant increase in oxygen vacancy content [10]. OER test results indicated that the treated samples exhibited improved catalytic activity. Zheng et al. treated the spinel-type Co_3O_4 sample in a $NaBH_4$ solution for 1 hour and found that the sample's activity increased post-treatment [11]. The oxygen vacancies introduced altered the electronic structure of the oxide, enhancing the catalytic reaction activity. $NaBH_4$ could be utilized as a reducing agent to create a large number of oxygen vacancy defects in FeCo oxide nanosheets, which improved the material's conductivity, increased the number of surface active sites, and significantly enhanced the catalytic reaction activity [12]. Furthermore, $NaBH_4$ can effectively prepare reduced $CoFe_2O_4$ nanosheets (NS) rich in oxygen vacancies, leading to more active sites and enhanced conductivity compared to the pristine $CoFe_2O_4$ hollow nanosphere [13]. These nanosheets achieved a current density of 10 mA cm^{-2} at an overpotential of 320 mV in 1 M KOH. As expected, the $CoFe_2O_4$ hollow nanosphere, with a relatively higher surface area after $NaBH_4$ reduction, showed the most notable improvement in OER activity, and the corresponding reduced $CoFe_2O_4$ NS demonstrated the best OER performance compared to the reduced $CoFe_2O_4$ bulk and nanoparticles.

Hydrogen reduction treatment is also an effective approach. Du et al. treated the obtained mesoporous $NiFe_2O_4$ material in a mixed gas (40% H_2/N_2) for 1 hour and controlled different reduction temperatures to generate more oxygen vacancies on the catalyst surface [14]. The presence of a large number of oxygen vacancies and active sites promotes the catalytic reaction, and the increase in defect states enhances the oxide's conductivity.

Additionally, more defects can be introduced into the spinel structure through electrochemical reduction, improving the material's conductivity and electrochemical active sites. The potential on the cathode can be accurately adjusted, and the reduction process of the cathode can be precisely controlled without introducing strong reducing agents during the electrolysis process. Wang et al. induced oxygen vacancies by reduction at a potential of −0.9 V (NCO-0.9@CC) [15]. During the electrochemical reaction process, oxygen vacancies act as active sites, promoting electron/ion transfer rates and achieving the goal of enhancing energy storage.

3.3 Etching method

The etching method can directly control oxygen defects on the surface of spinel. Dai et al. treated the prepared sample with Ar plasma and found that the surface area of the treated sample increased significantly [16]. Moreover, the current density corresponding to 1.6 V VS RHE was 44.44 $mA \cdot cm^{-2}$, with a lower starting potential. After plasma etching, the increased surface area and internal oxygen vacancy content of the sample contribute to the improved activity of the catalyst.

Oxygen vacancy-rich $FeCo_2O_4$ nanoparticles can also be prepared by laser treatment. These oxygen vacancies effectively reduce the thermodynamic energy barrier and expedite electron transfer, thereby simultaneously enhancing both the oxygen evolution and reduction reactions [17].

3.4 Doping method

Heteroatom doping is a low-cost and highly effective method for incorporating oxygen vacancies. N and P co-doping can cause the formation of oxygen vacancies and metal-nitrogen bonds, leveraging the use of ionic liquids as sources for N and P. This strategy results in superior catalytic performance in the activation of persulfate [18].

Stabilizing oxygen vacancies by filling with non-metallic elements with different atomic radii and electronegativities to compensate for the coordination number of metal elements is a viable strategy. For instance, using sulfur atoms to effectively stabilize oxygen vacancies and reduce the Bader charge of atoms near these vacancies is beneficial for the adsorption and desorption of intermediate products in the reaction [19]. It can also form cobalt-sulfur coordination with the cobalt active center adjacent to the oxygen vacancy, thereby regulating the electronic structure of the active center and increasing the H_2O adsorption energy on the cobalt active site.

Zeng et al. [20] introduced both oxygen vacancies and phosphorus ions into $NiCo_2O_4$ nanosheets, which initially had low conductivity and fewer active sites, resulting in significantly improved conductivity, rate performance, and capacity for the optimized P-$NiCo_2O_4$-x NS zinc-ion battery. Zhang et al. [21] constructed anionic defects on $NiCo_2O_4$ through a mechanochemical strategy involving Na-assisted milling for propane oxidation (**Figure 5a**). This process substantially improved the oxygen vacancies, active oxygen species, and oxygen mobility of the catalyst. Lu et al. [22] prepared a novel $CeO_2/MnCo_2O_4$ catalyst, with CeO_2 acting as a key substance for creating oxygen vacancies. The stability of methane catalytic oxidation in unmodified $MnCo_2O_4$ pure samples is poor, while the stability of oxidation–reduction in samples modified with CeO_2 is enhanced. This enhancement is attributed to the partial substitution of high-valence Ce^{4+} with low-valence cations (Mn^{3+}, Co^{2+}, and Co^{3+}), allowing them to be partially doped into the $MnCo_2O_4$ lattice and generate a large number of oxygen vacancies to maintain charge balance.

The incorporation of Ce into $CuFe_2O_4$ spinel lattice has been instrumental in facilitating electron exchange, bolstering the oxygen storage capacity, and fostering the formation of oxygen vacancies [23]. However, an excessive amount of Ce can diminish the specific surface area and occupy surface oxygen vacancies, leading to detrimental effects.

3.5 Composite method

The introduction of supplementary materials can also result in an elevation of oxygen vacancies within the spinel structure. Chuang et al. [24] synthesized a novel hybrid catalyst featuring $CoFe_2O_4$ nanorods encapsulated by single-walled carbon nanotubes (SWNTs). The synergistic effect between $CoFe_2O_4$ nanorods and SWNTs not only increases the oxygen vacancies and optimizes the electronic structure of the composite but also facilitates the adsorption and stabilization of hydroxyl groups, significantly improving both OER and HER performances.

The synergistic interaction between SWNTs and $CoFe_2O_4$ nanorods not only increases the oxygen vacancies and refines the electronic configuration of the composite, but also facilitates the adsorption and stabilization of hydroxyl groups, leading to a marked enhancement in both oxygen evolution reaction and hydrogen evolution reaction performances.

Additionally, the hollow $CoFe_2O_4$ nanocubes, which are carbon-coated and derived from Prussian blue analogs and feature an abundance of oxygen vacancies, have achieved remarkable results with an ammonia yield rate of 30.97 $\mu g{\cdot}h^{-1}{\cdot}mg_{cat.}^{-1}$ at −0.4 V versus the reversible hydrogen electrode in 0.1 M Na_2SO_4 [25].

4. Characterizations of oxygen vacancies

Various methods are available for characterizing oxygen vacancies. For instance, the distribution of oxygen vacancies can be directly observed through visualization techniques such as scanning tunneling microscopy (STM) and aberration-corrected scanning transmission electron microscopy (AC-STEM). Spectroscopic techniques like X-ray fine absorption spectroscopy (XAFS), electron paramagnetic resonance (EPR), X-ray diffraction (XRD), X-ray photoelectron spectroscopy (XPS), Raman spectroscopy, positron annihilation technique (PAT), and others can qualitatively or quantitatively provide information on oxygen vacancies. Moreover, density functional theory calculations (DFT) can theoretically predict the form and content of oxygen vacancies.

Determining the form, location, and concentration of defects in materials is essential for studying the influence of defect structure on the catalytic activity and stability of spinel. A range of physical and chemical characterization methods is required to study the location and content of defects, with spectroscopy being the primary method for defect characterization.

4.1 Raman spectroscopy

The application of Raman spectroscopy in oxygen defect analysis is extensive. Utilizing the Raman scattering effect, the technique analyzes the scattering spectra at various frequencies distinct from the incident light, thereby extracting insights into molecular vibrations and rotations and studying molecular structure. Raman spectroscopy can reveal structural changes in materials caused by oxygen vacancies or defects.

To verify the physical properties and further explore the structural defects of catalysts, Raman spectroscopy was performed. **Figure 2(a)** shows that $NiCo_2O_4$ exhibited typical Raman spectra at 655 cm^{-1} (A1g), 516 cm^{-1} (F2g), 468 cm^{-1} (Eg), and 186 cm^{-1} (F2g), consistent with the spinel vibrational modes. A noticeable blue shift of the main peak (644 cm^{-1}) for D-$NiCo_2O_4$, compared to $NiCo_2O_4$, sufficiently proves the presence of structural defects induced by lattice distortion in D-$NiCo_2O_4$ [26].

Raman spectroscopy was also used to study the structural characteristics of the $CuCo_2O_4$ spinel catalyst and surface defects, as shown in **Figure 2(b)**. The presence of two bands at 510 and 462 cm^{-1} is evident. The band at 510 cm^{-1} is attributed to the Cu-O stretching in the octahedral sites of Cu^{2+}-O^{2-}, while the Co-O stretching vibration in the tetrahedral sites of $Co^{3+} - O^{2-}$ is observed at 462 cm^{-1}. Meanwhile, the pronounced band at 651 cm^{-1} and the small band at 547 cm^{-1} are indicative of the $CuCo_2O_4$ spinel crystal structure [27].

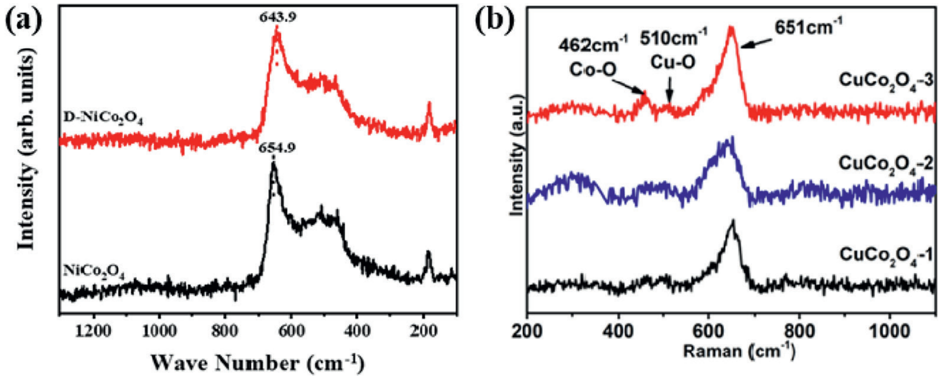

Figure 2.
(a) Raman spectra of $NiCo_2O_4$ *and D-*$NiCo_2O_4$*; (b) Raman spectra of* $CuCo_2O_4$*-1,* $CuCo_2O_4$*-2, and* $CuCo_2O_4$*-3.*

4.2 X-ray photoelectron spectroscopy (XPS)

XPS, a highly sensitive ultra-microscopic surface analysis technique, was commonly used in early research of defect chemistry to characterize defects in catalysts. It identifies defect types or concentrations by analyzing surface peak positions, valence bond changes, and bonding information [28, 29].

As shown in **Figure 3(a)**, the O 1 s spectrum of $NiCo_2O_4$ was fitted into O1, O2, and O3 with binding energies of 529.6, 531.2, and 532.6 eV, respectively. The O1 peak is attributed to the oxygen-metal bonds, specifically the interactions between oxygen and metals such as Co or Ni (O-Co/Ni). The O2 peak is likely associated with defective oxygen structures that exhibit low coordination numbers. Meanwhile, the O3 peak corresponds to oxygen species that are part of adsorbed water molecules [30]. It is evident that there is a significant increase in O2 for D-$NiCo_2O_4$, certifying the successful introduction of oxygen vacancies. The oxygen vacancy structure significantly influences the catalytic oxidation reaction by transforming O_2 molecules into active

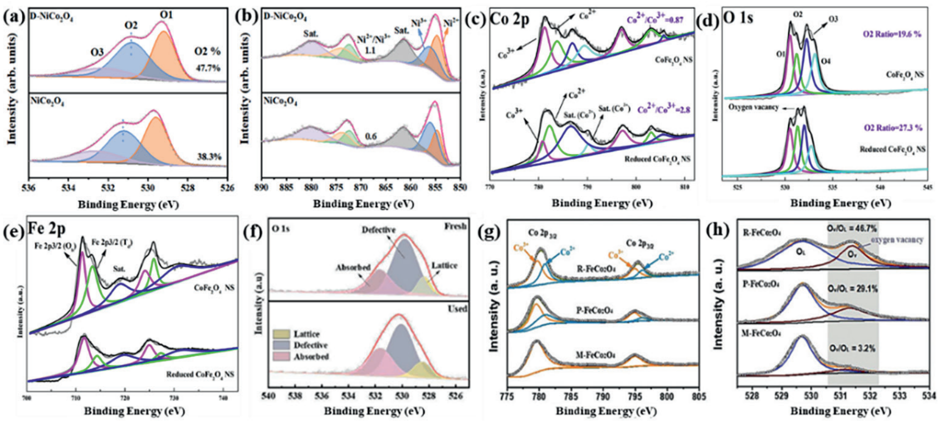

Figure 3.
XPS spectra of (a) O 1 s, (b) Ni 2p for $NiCo_2O_4$*, and D-*$NiCo_2O_4$*; XPS spectra of (c) Co 2p, (d) O 1 s, and (e) Fe 2p for the pristine* $CoFe_2O_4$ *hollow nanospheres and the reduced* $CoFe_2O_4$ *nanosheet; (f) O 1 s XPS spectrum of CFB-2 before and after the reaction; the fitted (g) Co 2p and (h) O 1 s spectra of different* $FeCo_2O_4$ *samples.*

surface oxygen and increasing oxygen mobility. In **Figure 3(b)**, the Ni 2p3/2 spectrum could be decomposed into the doublets of spin-orbits, with peaks corresponding to Ni^{2+} at 854.6 eV and Ni^{3+} at 855.9 eV, respectively [26]. The ratio of Ni^{2+}/Ni^{3+}, as well as Co^{2+}/Co^{3+}, in the defect-engineered D-$NiCo_2O_4$ is notably higher than that observed in the pristine $NiCo_2O_4$. The significant increase suggests that the defects engineering process could effectively reduce state of the metal ions. This correlates with the higher proportion of oxygen vacancies in D-$NiCo_2O_4$, created to balance the valence state. Interestingly, the Ni^{2+}/Ni^{3+} ratio exhibits a more pronounced increase compared to that of Co^{2+}/Co^{3+}, indicating that Ni^{3+} ions are more readily reduced than Co^{3+} ions.

The deficiencies in the reduced $CoFe_2O_4$ NS and its corresponding pristine $CoFe_2O_4$ hollow nanospheres were then characterized by XPS [13]. As shown in **Figure 3(c)**, the Co 2p spectra of hollow $CoFe_2O_4$ nanospheres and reduced $CoFe_2O_4$ NS are well fitted to 7 components, indicating the coexistence of Co^{2+} and Co^{3+} in $CoFe_2O_4$. The Co^{2+}/Co^{3+} ratio on the surface of the hollow $CoFe_2O_4$ nanospheres is 0.87, while that for the reduced $CoFe_2O_4$ NS is as high as 2.8. This significant increase suggests that the reduction process has led to a substantial enrichment of Co^{2+} species on the surface of the $CoFe_2O_4$ NS [12]. As evidenced by the detailed deconvolution of the O 1 s spectra, the reduction process involving $NaBH_4$ has been shown to generate a higher concentration of oxygen vacancies on the surface of $CoFe_2O_4$. **Figure 3(d)** illustrates the O 1 s region, which can be deconvoluted into four distinct oxygen peaks. The O1 peak, centered at approximately 529.7 eV, corresponds to metal-oxygen bonds. The O2 peak, observed at a higher binding energy of 531.2 eV, is characteristic of oxygen defect sites. The O3 peak, positioned at around 532.5 eV, is indicative of surface-adsorbed oxygen or hydroxyl groups. Lastly, the O4 peak at 533.4 eV is associated with adsorbed molecular water, as referenced in [12]. As shown in **Figure 3(e)**, the Fe 2p spectra are characterized by two shakeup satellites at 718.1 and 732.8 eV, along with two spin-orbit doublet peaks corresponding to Fe 2p3/2 and Fe 2p1/2. The XRD and XPS analyses suggest that the $NaBH_4$ reduction method is an efficient and reliable approach for preparing homogeneous metal oxides that are rich in oxygen vacancies.

As further observed in **Figure 3(f)**, there is a noticeable decrease in the relative peak area ratio between defect oxygen and lattice oxygen. This reduction primarily stems from the reaction of oxygen vacancies on the catalyst surface with dissolved oxygen in water, leading to the formation of metastable intermediates (O_V-O*) [31]. These intermediates serve as activation centers that facilitate the production of reactive oxygen species (ROS), particularly $\bullet O_2^-$ and $^1O_2$. The oxygen vacancies present on the surface of the $CoFe_2O_4$-loaded biochar composite (CFB-2) partially contribute to $^1O_2$ generation through their transformation into metastable intermediates with dissolved oxygen. To elucidate the enhanced performance of R-$FeCo_2O_4$, XPS measurements were conducted on three $FeCo_2O_4$ samples. **Figure 3(g)** presents the O 1 s spectra, which can be deconvoluted into two peaks at 529.7 and 531.3 eV. The peak at 529.7 eV is associated with lattice oxygen (O_L), while the peak at 531.3 eV corresponds to adsorbed oxygen on an oxygen vacancy (O_V) [17]. It is evident that the OV/OL ratio for R-$FeCo_2O_4$ (46.7%) is significantly higher than that of P-$FeCo_2O_4$ (29.1%) and M-$FeCo_2O_4$ (3.2%), indicating that laser fragmentation has generated a greater number of oxygen vacancies in R-$FeCo_2O_4$. The high-resolution Co 2p XPS spectra depicted in **Figure 3(h)** reveal that the majority of cobalt cations in the $FeCo_2O_4$ samples are in the Co^{3+} state. However, R-$FeCo_2O_4$ exhibits a more pronounced peak related to Co^{2+} ions compared to the other samples, and Co^{2+} ions have been identified as the catalytically active sites for the ORR.

4.3 Electron paramagnetic resonance (EPR) spectra

EPR is a magnetic resonance technique based on the magnetic moment of unpaired electrons, which is capable of both qualitatively and quantitatively detecting unpaired electrons within material atoms. It offers insights into the structural characteristics and immediate surroundings. EPR characterization is instrumental in confirming the presence of oxygen vacancies, providing valuable information about their formation and distribution within the material. As depicted in **Figure 4(a)**, D- $NiCo_2O_4$ exhibits a pronounced EPR signal, with a peak intensity approximately 4.1 times greater than that of $NiCo_2O_4$, at a g-value of 1.99975. This signal is indicative of paramagnetic oxygen vacancies within the spinel oxide structure, thereby robustly confirming that the mechanochemical process has successfully introduced a substantial number of oxygen vacancies into $NiCo_2O_4$ [26]. In **Figure 4(b)**, all $CuCo_2O_4$-1, $CuCo_2O_4$-2, and $CuCo_2O_4$-3 exhibited an EPR signal centered at approximately 3360, which can be ascribed to the surface electrons that are trapped at the oxygen vacancy sites. The highest intensity of EPR signal for $CuCo_2O_4$-3 suggests the most oxygen vacancies on the surface [27]. The oxygen vacancies present on the surface of the $CoFe_2O_4$-loaded biochar composite (CFB-2) play a partial role in generation of $^1O_2$ by transforming into a metastable intermediate in conjunction with dissolved oxygen.

The asymmetric stretching vibration of the Fe/Co-O bond, characteristic of the T2g mode, was detected at the tetrahedral position in the CFB-2 catalyst, signifying a substantial presence of oxygen vacancies (OVs). Concurrently, a pronounced asymmetric signal at g = 2.003 is distinctly visible in **Figure 4(c)**, which is indicative of the trapping of unpaired electrons within these oxygen vacancies. The underlying mechanism involves electron-rich groups on the biochar (BC) acting as Lewis bases to mediate electron transfer, thereby initiating a redox reaction that leads to the formation of singlet oxygen ($^1O_2$). The metastable intermediates created by OVs effectively reduce the O-O bond strength, resulting in a significant production of reactive oxygen species (ROS). Additionally, a high-valent metal ion formed through

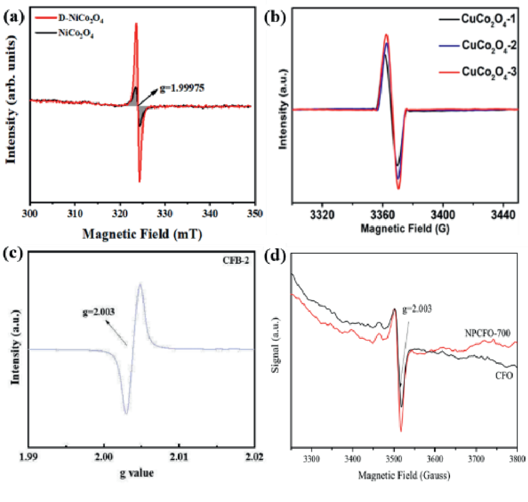

Figure 4.
(a) EPR spectra for $NiCo_2O_4$ and D-$NiCo_2O_4$; (b) EPR spectra of $CuCo_2O_4$-1, $CuCo_2O_4$-2, and $CuCo_2O_4$-3; (c) the EPR spectra of CFB-2 before and after the reaction; (d) EPR spectra of CFO and NPCFO-700.

a two-electron transfer process aids in the electron transfer to superoxide (•O_2^-), facilitating the generation of $^1O_2$.

In-situ EPR analysis was utilized to further elucidate the disparity in oxygen vacancy concentration between CFO and NPCFO-700, as shown in **Figure 4(d)**. It has been documented that the EPR resonance signal with a g value of 2.003 corresponds to the free spins induced by OVs and is directly proportional to the OV concentration [32]. In this context, the EPR signal intensity of NPCFO-700 was more intense than that of CFO, suggesting a higher concentration of oxygen vacancies in NPCFO-700 compared to other NPCFP-x samples.

5. Analysis of the mechanism of spinel oxygen defects

Oxygen vacancies can significantly adjust the electron density around the Fermi level, effectively forming and transforming reaction intermediates. They can effectively regulate the structure and electronic properties of spinel, adjust electronic configurations, and change the center position of the d-band of metal oxides, enhancing the surface adsorption/desorption ability of catalysts and optimizing electrocatalytic kinetics and catalytic activity. Theoretical studies have shown that vacancy modification increases the active sites and reduces the catalytic energy barrier, lowers the Gibbs free energy at the basic reaction level, and ultimately improves its electrocatalytic performance [33–38].

As shown in **Figure 5(a)**, to certify the enhancement of DCM dichlorination reaction activity on $CuCo_2O_4$ (311) and $CuCo_2O_4$-O_V, DFT calculations were carried out to investigate the active sites and catalytic mechanism. It is worth noting that the

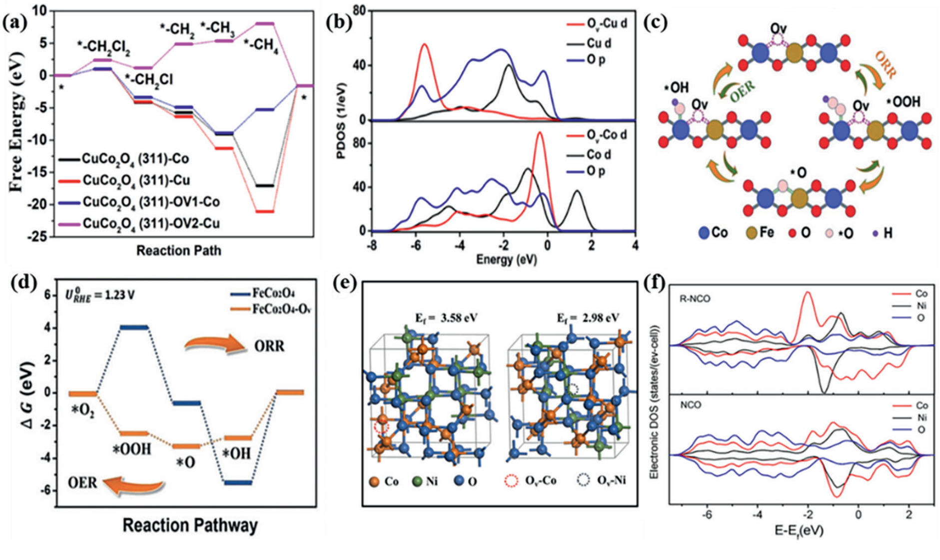

Figure 5.
(a) Reaction energy barrier for the dechlorination of DCM to CH_4 on $CuCo_2O_4$ catalysts; (b) Curves of projected density of states of Co d, Cu d, and O p orbitals for $CuCo_2O_4$ (311) and $CuCo_2O_4$ (311)-O_v; (c) The reaction mechanism of R-$FeCo_2O_4$ with O_V; (d) The DFT diagram of pristine $FeCo_2O_4$ and R-$FeCo_2O_4$; (e) O_v formation energy (E_f) induced by the reduction of Co, Ni, and the corresponding crystal structure; (f) Calculated DOS curves for pristine NCO and R-NCO.

second dechlorination step (from $* - CH_2Cl$ to $* - CH_2$) is the potential limiting step for $CuCo_2O_4$ (311)-O_V-Cu, which shows the lowest energy barrier.

The results indicate that the $CuCo_2O_4$ (311)-O_V-Cu is the most active site for the dechlorination of CH_2Cl_2 into CH_4. The projected density of states (PDOS) plots, as depicted in **Figure 5(b)**, elucidate the intricate electronic interactions that occur between the adsorbates and the catalysts. Notably, they reveal a significant reduction in the d-band center for O_V-Cu, which leads to weaker binding between the $^*CH_4$ intermediate and $CuCo_2O_4$ (311)-O_V-Cu, and further improvement in dechlorination performance [27].

Subsequently, they conducted DFT calculations to dissect the impact of oxygen vacancies on the catalytic mechanism. Both the OER and the ORR encompass four fundamental reaction steps, as illustrated in **Figure 5(c)**. During the ORR, O_2 molecules are adsorbed onto the catalyst surface and sequentially reduced to *OOH, *O, *OH, and ultimately H_2O. Conversely, the OER occurs in the opposite direction. The free energy diagrams derived from DFT calculations are portrayed in **Figure 5(d)**, where a substantial thermodynamic barrier (ΔG) is observed for the formation of *OOH on the pristine $FeCo_2O_4$ surface devoid of oxygen vacancies. Upon introducing oxygen vacancies into R- $FeCo_2O_4$, this ΔG value is markedly diminished, thereby enhancing the efficiency of both the ORR and OER processes. The substantially reduced ΔG values for the reduction of *O to *OOH and *OOH to O_2 indicate a higher catalytic efficiency for the four-electron dominant process, which is corroborated by the K-L plot results. Consequently, the DFT findings underscore the pivotal role of oxygen vacancies in augmenting the catalytic activities of $FeCo_2O_4$ for both ORR and OER [17].

The DFT calculations also assessed the formation energy (Ef) of oxygen vacancy structures (O_V-Ni and O_V-Co) associated with the reduction of Ni^{3+} and Co^{3+}, respectively. As depicted in **Figure 5(e)**, the formation energy for O_V-Ni is notably lower than that for O_V-Co, effectively substantiating the enhancement of reducibility and oxygen vacancy formation due to the incorporation of Ni into the spinel structure [26].

The extensive study, encompassing both experimental analyses and theoretical computations, has revealed the presence of single-site oxygen vacancies (SSOVs) and their role in enhancing the dissociation of N-O bonds in catalytic reactions. In the context of the rate-determining step for the NO+CO reaction on CO-$CuMn_2O_4$, we conducted density functional theory (DFT) calculations to compare the reaction pathways on CO-CuO and CO-Mn_2O_3.

As illustrated in **Figure 6(a)**, the computational models for SSOVs on mono-component catalysts are depicted as CO-CuO (111) and CO-Mn_2O_3 (111). On the CO-CuO (111) surface, CO and NO molecules are capable of adsorbing onto the copper site in proximity to the oxygen vacancy. However, the energy barrier for the transition state TS1' is exceedingly high at 2.31 eV, which confines the nitrogen atom (N*) to the surface, rendering it incapable of occupying the oxygen vacancy in the subsequent reaction step. A comparable situation arises in the reduction of NO by CO on the CO-Mn_2O_3(111), where the energy barrier for the transition state TS1" is also notably high at 2.20 eV. This barrier prevents the N* atom from directly filling the oxygen vacancy on the CO-Mn_2O_3(111) surface. Furthermore, as shown in **Figure 6(b-f)**, crystal orbital Hamilton population (COHP) analyses were performed for the CO-$CuMn_2O_4$(100), CO-CuO(111), and CO-Mn_2O_3(111) surfaces. In COHP analysis, negative values typically indicate bonding interactions, while positive values denote antibonding interactions. The analysis of the Integrated Crystal Orbital Hamilton Population (ICOHP) values for the N-O bonds in **Figure 6(b-d)** suggests that the difficulty in breaking the N-O bond should be ranked as CO-Mn_2O_3(111) > C

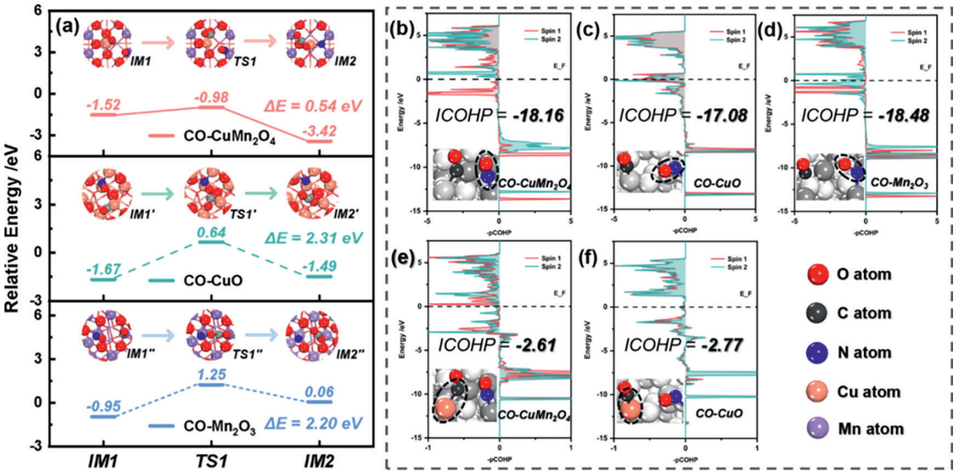

Figure 6.

(a) Energy comparison of key steps of the NO + CO reaction on CO-$CuMn_2O_4$ *(100), CO-CuO(111), and CO-*Mn_2O_3*(111) surfaces, (b-d) the ICOHP results of the N-O bond over (b) CO-*$CuMn_2O_4$ *(100), (c) CO-CuO(111), (d) CO-*Mn_2O_3*(111) surfaces, (e, f) the ICOHP results of Cu and C atoms over, (e) CO-*$CuMn_2O_4$*(100), and (f) CO-CuO(111) surfaces.*

O-$CuMn_2O_4$(100) > CO-CuO(111). Theoretically, a higher difficulty in breaking the N-O bond would impede the reaction progress. However, upon scrutinizing the energy barriers associated with the pivotal step (*N-O + Cu-*CO → *N + CO_2) as depicted in **Figure 6(a)**, it can be deduced that the reaction activity on the four catalysts follows the order of CO-$CuMn_2O_4$(100) < CO-Mn_2O_3(111) < CO-CuO(111).

In practice, for the NO + CO reactions on CO-CuO(111) and CO-$CuMn_2O_4$(100) surfaces, CO must undergo migration from Cu sites to the adsorbed NO, and the dissociation of the Cu-C bond during this transition could significantly influence the energy barrier of TS1. The ICOHP values presented in **Figure 6(e, f)** suggest that the strength of the Cu-C bond on the CO-$CuMn_2O_4$(100) surface is weaker than that on CO-CuO(111), which facilitates CO migration on the CO-$CuMn_2O_4$(100) catalyst surface and enhances its reactivity with NO. Consequently, the bond strength of the Cu-C is a pivotal factor that warrants consideration, in addition to the N-O bond strength of adsorbed NO. Moreover, the adsorption capacity for CO molecules is limited on the CO-Mn_2O_3(111) surface, which is detrimental to the subsequent NO + CO reaction.

The exhaustive investigation, encompassing both experimental characterizations and theoretical computations, has unveiled the presence of SSOVs and their pivotal role in facilitating the dissociation of N-O bonds during catalytic reactions. To gain insights into the rate-limiting step of the NO+CO reaction on CO-$CuMn_2O_4$, we conducted DFT simulations of analogous reaction pathways on CO-CuO and CO-Mn_2O_3. As depicted in **Figure 6(a)**, the computational models for single-component catalysts featuring SOVs are exemplified by CO-CuO(111) and CO-Mn_2O_3(111). Both CO and NO molecule adsorb preferentially at Cu sites adjacent to OVs on the CO-CuO(111) surface. However, the transition state of TS1' encounters a formidable energy barrier of 2.31 eV, which confines the N* atom to the surface, preventing it from occupying the oxygen vacancy in the subsequent steps. In similar, the reduction of NO by CO on CO-Mn_2O_3(111) mirrors this trend, with an equally steep energy barrier of 2.20 eV for TS1", hindering direct occupation of the oxygen vacancy by the N* atom.

Furthermore, **Figure 6(b-f)** presents crystal orbital Hamilton population (COHP) analyses for CO-$CuMn_2O_4$(100), CO-CuO(111), and CO-Mn_2O_3(111) surfaces. In COHP, negative values signify bonding interactions, whereas positive values indicate antibonding. Analyzing the ICOHP values for N-O bonds in **Figure 6(b-d)** suggests that the difficulty of N-O bond cleavage follows the order: CO-Mn_2O_3(111) > CO-$CuMn_2O_4$(100) > CO-CuO(111). Theoretically, this order implies a corresponding increase in reaction difficulty. Nevertheless, contrasting the energy barriers for the crucial step (N-O + Cu-CO → *N + CO_2) in **Figure 6(a)** reveals a contrasting trend: CO-$CuMn_2O_4$(100) < CO-Mn_2O_3(111) < CO-CuO(111). Notably, for reactions on CO-CuO(111) and CO-$CuMn_2O_4$(100), the migration of CO from Cu sites to the adsorbed NO is essential, and the disruption of the Cu-C bond during this migration can significantly modulate the energy barrier at TS1. The ICOHP values depicted in **Figure 6(e, f)** suggest that the Cu-C bond on the surface of CO-$CuMn_2O_4$(100) is comparatively weaker, facilitating CO migration and enhancing its reactivity with NO. Thus, the Cu-C bond strength, in addition to the N-O bond strength of adsorbed NO, is a crucial factor influencing the TS1 energy barrier. Lastly, the limited CO adsorption capacity on CO-Mn_2O_3(111) hinders the subsequent NO+CO reaction.

6. Conclusions

In summary, oxygen vacancies in spinel oxides are a crucial factor influencing their structural and functional properties. These vacancies, which can be introduced through various methods such as heat treatment, chemical reduction, etching, doping, and composite formation, significantly alter the material's physical properties like conductivity, redox capability, and catalytic activity. They provide active sites, enhance electron/ion transfer rates, and lower reaction activation energies, thereby improving the overall performance of spinel oxides in catalytic reactions. Characterization techniques provide insights into the distribution, concentration, and nature of oxygen vacancies. For example, XPS can reveal changes in the oxidation states of metal ions and the presence of defective oxygen structures, while EPR can confirm the presence of unpaired electrons associated with oxygen vacancies. Theoretical calculations, such as DFT, further support the experimental findings by illustrating the role of oxygen vacancies in modifying the electronic structure of spinel oxides and facilitating catalytic reactions.

Acknowledgements

We acknowledge the support of the Fundamental Research Funds for the Central Universities (Nos. 310400209508 and 311324240543) and the National Natural Science Foundation of China (No. 22472009) for their financial support of this work.

Author details

Jiacheng Li
School of Environment, Beijing Normal University, China

*Address all correspondence to: ljc@bnu.edu.cn

References

[1] Ming ZH, Jin YZ, Wen JZ. Synthesis of oxygen vacancy-enriched N/P co-doped $CoFe_2O_4$ for high-efficient degradation of organic pollutant: Mechanistic insight into radical and nonradical evolution. Environmental Pollution. 2021;**270**:116092-116103. DOI: 10.1016/j.envpol.2020.116092

[2] Song J, Wei C, Huang ZF, Chuntai L, Lin Z, Xin W, et al. A review on fundamentals for designing oxygen evolution electrocatalysts. Chemical Society Reviews. 2020;**49**:2196-2214. DOI: 10.1039/C9CS00607A

[3] Zhang N, Li X, Ye H, et al. Oxide defect engineering enables to couple solar energy into oxygen activation. Journal of the American Chemical Society. 2016;**138**:8928-8935. DOI: 10.1021/jacs.6b04629

[4] Liu Y, Zhang N, Yu C, et al. $MnFe_2O_4$@C nanofibers as high-performance anode for sodium-ion batteries. Nano Letters. 2016;**16**:3321-3328

[5] Li C, Han XP, Cheng FY, et al. Phase and composition controllable synthesis of cobalt manganese spinel nanoparticles towards efficient oxygen electrocatalysis. Nature Communications. 2015;**6**:7345

[6] Wang XT, Ouyang T, Wang L, et al. Surface reorganization on electrochemically-induced Zn-N-Co spinel oxides for enhanced oxygen electrocatalysis. Angewandte Chemie International Edition. 2020;**59**:6492-6499

[7] Bao J, Zhang XD, Fan B, et al. Ultrathin spinel-structured nanosheets rich in oxygen deficiencies for enhanced electrocatalytic water oxidation. Angewandte Chemie. 2015;**127**:7507-7512

[8] Wei C, Feng ZX, Scherer GG, et al. Cations in octahedral sites: A descriptor for oxygen electrocatalysis on transition-metal spinels. Advanced Materials. 2017;**29**:1606800

[9] Chen S, Huang D, Liu D, et al. Hollow and porous $NiCo_2O_4$ nanospheres for enhanced methanol oxidation reaction and oxygen reduction reaction by oxygen vacancies engineering. Applied Catalysis B: Environmental. 2021;**291**:120065

[10] Sahoo P, Tan JB, Zhang ZM, et al. Engineering the surface structure of binary/ternary ferrite nanoparticles as high-performance electrocatalysts for the oxygen evolution reaction. ChemCatChem. 2018;**10**:1075-1083

[11] Wang YC, Zhou T, Zheng GF. Reduced mesoporous Co_3O_4 nanowires as efficient water oxidation electrocatalysts and supercapacitor electrodes. Advanced Energy Materials. 2014;**4**:1400696

[12] Zhuang LZ, Ge L, Yang YS, et al. Ultrathin iron-cobalt oxide nanosheets with abundant oxygen vacancies for the oxygen evolution reaction. Advanced Materials. 2017;**29**:1606793-1606799

[13] Kai LY, Xiao S, Zhang L, Bin D, Shan SL, Jing QC, et al. A facile method for reduced $CoFe_2O_4$ nanosheets with rich oxygen vacancies for efficient oxygen evolution reaction. International Journal of Hydrogen Energy. 2017;**42**:24150-24158. DOI: 10.1016/j.ijhydene.2017.07.165

[14] Yue QD, Liu C, Wan YY, et al. Defect engineering of mesoporous nickel ferrite and its application for highly enhanced water oxidation catalysis. Journal of Catalysis. 2018;**358**:1-7

[15] Wang N, Zhao P, Zhang Q, et al. Monodisperse nickel/cobalt oxide composite hollow spheres with mesoporous shell for hybrid supercapacitor: A facile fabrication and excellent electrochemical performance. Composites Part B: Engineering. 2017;**13**:144-151

[16] Xu L, Jiang QQ, Xiao ZH, et al. Plasma-engraved Co_3O_4 nanosheets with oxygen vacancies and high surface area for the oxygen evolution reaction. Angewandte Chemie. 2016;**55**:5277-5281

[17] Kang WQ, Cong X, Yan Z, Rui ZL, Gu RS, Hui L, et al. Laser-induced oxygen vacancies in $FeCo_2O_4$ nanoparticles for boosting oxygen evolution and reduction. Chemical Communications. 2019;**55**:8579-8582

[18] Sun J, Guo N, Shao Z, Huang K, Li Y, He F, et al. A facile strategy to construct amorphous spinel-based electrocatalysts with massive oxygen vacancies using ionic liquid dopant. Advanced Energy Materials. 2018;**8**:1800980

[19] Wei X, Na Y, Xiao L, et al. 3D atomic-scale imaging of mixed Co-Fe spinel oxide nanoparticles during oxygen evolution reaction. Nature Communications. 2022;**13**:179

[20] Zeng YX, Lai ZZ, Lu XH, et al. Oxygen-vacancy and surface modulation of ultrathin nickel cobaltite nanosheets as a high-energy cathode for advanced Zn-ion batteries. Advanced Materials. 2018;**30**:1802396-1802403

[21] Zhang M, Sui X, Zhang X, Niu M, Li C, Wan H, et al. Multi-defects engineering of $NiCo_2O_4$ for catalytic propane oxidation. Applied Surface Science. 2022;**600**:154040

[22] Lu C, Deng R, Xu R, et al. Design of hybrid oxygen carriers with CeO_2 particles on $MnCo_2O_4$ microspheres for chemical looping combustion. Chemical Engineering Journal. 2021;**404**:126554

[23] Wang Y, Xue R, Zhao C, Liu F, Liu C, Han F. Effects of Ce in the catalytic combustion of toluene on $Cu_xCe_{1-x}Fe_2O_4$. Colloid. Surface. A. 2018;**540**:90-97

[24] Chuang W, Liang LG, Sheng You Q, Jian G, Yong Chao Z, Ke XW, et al. Modulating $CoFe_2O_4$ nanocube with oxygen vacancy and carbon wrapper towards enhanced electrocatalytic nitrogen reduction to ammonia. Applied Catalysis B: Environmental. 2021;**297**:120452-120462. DOI: 10.1016/j.apcatb.2021.120452

[25] Yu D, Jun Z, Wenqing Z, Jian Z, Xijie C, Fengchun Y, et al. Single-walled carbon nanotubes wrapped $CoFe_2O_4$ Nanorods with enriched oxygen vacancies for efficient overall water splitting. ACS Applied Energy and Materials. 2019;**2**:1026-1032

[26] Ming CZ, Xin S, Xin Z, Mang N, Cui QL, Hai QW, et al. Multi-defects engineering of $NiCo_2O_4$ for catalytic propane oxidation. Applied Surface Science. 2022;**600**:154040-154048. DOI: 10.1016/j.apsusc.2022.154040

[27] Jing W, Shi YF, Xin YL, Zhao DN, Zhi YL, Chun PB, et al. Rod-like nanostructured Cu-Co spinel with rich oxygen vacancies for efficient electrocatalytic dechlorination. ACS Applied Materials and Interfaces. 2023;**15**:12915-12923. DOI: 10.1021/acsami.2c19134

[28] Kumar M, Yun JH, Bhatt V, et al. Role of Ce^{3+} valence state and surface oxygen vacancies on enhanced electrochemical performance of single step solvothermally synthesized CeO_2 nanoparticles. Electrochimica Acta. 2018;**284**:709

[29] Ma L, Chen S, Pei Z, et al. Flexible waterproof rechargeable hybrid zinc batteries initiated by multifunctional oxygen vacancies-rich cobalt oxide. ACS Nano. 2018;**12**:8597-8605

[30] Bao J, Zhang X, Fan B, Zhang J, Zhou M, Yang W, et al. Ultrathin spinel-structured nanosheets rich in oxygen deficiencies for enhanced electrocatalytic water oxidation. Angewandte Chemie International Edition. 2015;**54**:7399-7404

[31] Shuo L, Ying NL, He SZ, Jun FN, Yoong KL, Duu JL, et al. Biochar loaded with $CoFe_2O_4$ enhances the formation of high-valent Fe(IV) and Co(IV) and oxygen vacancy in the peracetic acid activation system for enhanced antibiotic degradation. Bioresource Technology. 2023;**387**:129536-129546. DOI: 10.1016/j.biortech.2023.129536

[32] Gao P, Tian X, Nie Y, Yang C, Zhou Z, Wang Y. Promoted peroxymonosulfate activation into singlet oxygen over perovskite for ofloxacin degradation by controlling the oxygen defect concentration. Chemical Engineering Journal. 2019;**359**:828-839

[33] Hu Y, Lu W, Yan L, et al. Defect engineering of electrode materials towards superior reaction kinetics for high-performance supercapacitors. Journal of Materials Chemistry A. 2022;**10**:15267-15296

[34] Vazhayil A, Thomas N. Probing the electrocatalytic activity of hierarchically mesoporous M-Co_3O_4 (M= Ni, Zn, and Mn) with branched pattern for oxygen evolution reaction. Journal of Electroanalytical Chemistry. 2023;**934**:117298-117310

[35] Sheng JP, Feng G, Lin LL, De SY, Dong XJ, Tian RZ, et al. Necklace-like multishelled hollow spinel oxides with oxygen vacancies for efficient water electrolysis. Journal of American Chemical Society. 2018;**140**:13644-13653. DOI: 10.1021/jacs.8b05134

[36] Yu Z, Dan S, Yi XW, Xiao QL, Hong MS, Tong HC, et al. Facile electrochemically induced vacancy modulation of $NiCo_2O_4$ cathode toward high-performance aqueous Zn-based battery. Chemical Engineering Journal. 2023;**453**:139736-139745. DOI: 10.1016/j.cej.2022.139736

[37] Xiao LX, Xue QL, Long FM, Na NL, Shan Y, Hao L, et al. Construction of surface synergetic oxygen vacancies on $CuMn_2O_4$ spinel for enhancing NO reduction with CO. ACS Catalysis. 2024;**14**:3028-3040. DOI: 10.1021/acscatal.3c05337

[38] Fei X, Yi AW, Gui LX, Fei Y, Shang QZ, Cheng JS, et al. Fe–N–C boosts the stability of supported platinum nanoparticles for fuel cells. Journal of American Chemistry Society. 2022;**144**:20372-20384. DOI: 10.1021/jacs.2c08305